Molecular dynamics studies of ion beam implantation and patterning of silicon: Effect of noble gas cluster formation

Michael A. Lively,[1,2] Samuel X. Bennett,[1] and Jean Paul Allain[1,2,3,*]

[1]*Department of Nuclear, Plasma, and Radiological Engineering, University of Illinois at Urbana-Champaign, Urbana, Illinois 61802, USA*
[2]*Micro and Nanotechnology Laboratory, University of Illinois at Urbana-Champaign, Urbana, Illinois 61802, USA*
[3]*Beckman Institute for Advanced Science and Technology, University of Illinois at Urbana-Champaign, Urbana, Illinois 61802, USA*

(Received 19 April 2017; revised manuscript received 7 May 2018; published 26 June 2018)

The use of energetic ion beams to induce nanopattern formation at surfaces has been well studied both experimentally and theoretically. However, the influence on morphological evolution of the implanted species themselves remains little understood, particularly in the case when the incident ion species does not interact chemically with the target material. In this work, MD simulation results are presented for cumulative ion bombardment of Si to a fluence of 3×10^{15} cm^{-2} or more for a range of incident ion energies (20–1000 eV), angles ($0-85^{\circ}$), and species (Ne, Ar, Kr, Xe). For most cases, the implanted ions are observed to form gas clusters or bubbles beneath the surface as the fluence increases. The implantation and cluster formation decrease in magnitude with increasing ion incidence angle, and remain fairly similar for the heavier-than-Si species (Ar, Kr, and Xe). However, the implantation and cluster formation are much more prominent for Ne irradiation. As the fluence continues to increase beyond $\sim 10^{15}$ cm^{-2}, the gas clusters begin to become exposed to the vacuum as the Si layers trapping the gas atoms are eroded by the incident ions. The exposed gas clusters then degas very rapidly, leading to disruption at the surface and to viscous material flow of Si into the void left behind. Comparison to dynamic binary collision approximation (BCA) simulations indicates that cluster formation and degassing contributes to a wide distribution of single-impact emission yields of implanted ions, contrary to intuitive expectations based on BCA simulations. Notably, the increased size and frequency of many-atom implanted ion emission events contributes to a much lower concentration of the implanted species than is otherwise expected from BCA simulations. Additionally, this cluster degassing phenomenon is conjectured to provide a potential "antipatterning" mechanism by disrupting or destroying nanopattern "seeds" at the surface. This could provide an additional mechanism to improve model predictions of critical angles for patterning transitions, and may also provide at least a partial explanation for the difficulty of obtaining patterns on Ne-bombarded Si surfaces.

DOI: 10.1103/PhysRevB.97.235443

I. INTRODUCTION

The use of low-energy ($\leqslant 1$ keV) ion beams to induce pattern formation on silicon surfaces is a well-established, extensively explored technique offering substantial promise for efficient, scalable fabrication of Si nanostructures for advanced materials and device applications [1]. Depending on the experimental setup and ion beam properties, patterns that can be grown on Si include ripples, dots, holes, various superpositions of these, or even a simple flat surface [2]. For the relatively simple case of a single beam incident on a stationary Si surface, it has been established by experiments [3,4] that ripples form above some critical angle, $\theta_c > 45^{\circ}$, with a wave vector oriented parallel to the projected ion beam direction along the surface. Furthermore, the orientation of these ripples can rotate by 90° for grazing incidence angles, introducing a second critical angle into the system. For near-normal incidence, however, the Si surface remains flat in the absence of impurities.

There have been numerous theoretical efforts to explain and predict the range of morphologies for this "simple" experimental system. The most widely applied theory of ion beam patterning is that of Bradley and Harper [5], which proposes curvature-dependent sputtering as the driving mechanism behind ion beam patterning. The Bradley-Harper model has, in turn, provided the basis for the majority of expanded theoretical treatments addressing high-fluence phenomena, such as annealing of defects, pattern coarsening, and dynamic scaling of the interface width [6]. The Bradley-Harper model predicts the transition from parallel-mode to perpendicular-mode ripples, but also predicts that the surface is unstable under all conditions, and is thus unable to explain the existence of flat surfaces. An alternative mechanism of ion-induced mass redistribution was first proposed by Carter and Vishnyakov [7], and this was shown to be able to predict the flat-to-rippled transition at 45° incidence, but did not predict the parallel-to-perpendicular mode transition. More recently, models describing the surface evolution in terms of ion-enhanced viscoelastic flow of an amorphous surface layer have been more successful at predicting the quantitative properties of the ripples [8–10], but still neglect the grazing-incidence transition.

Computer simulations have also been used to better understand the driving mechanisms behind ion-induced patterning of Si, ranging from atomistic simulations using molecular dynamics (MD) to long-time kinetic Monte Carlo (kMC) models of the whole-surface evolution. In particular, MD simulations have been used to study the sputtering behavior [11–13] point defect production mechanisms [14,15],

*allain@illinois.edu

 ©2018 American Physical Society

amorphization/recrystallization mechanisms [16–18], and the ion implantation profile [15,19]. Meanwhile, kMC simulations have been used to study the influence of various mechanisms on the pattern formation, with an emphasis on various surface diffusion mechanisms [20–24]. However, these simulations have not generally been well integrated with theoretical models until fairly recently.

In the past several years, substantial efforts have been made to integrate the results of simulations with theoretical models and experimental measurements. The work of Norris and coworkers [25], while not without serious flaws [26,27], has motivated the development and extension of the so-called "crater function" formalism, where statistical information about the surface response to single-ion impacts provides the basis for calculating the curvature coefficients. This formalism has been used in a mathematically expanded form coupled to crater functions obtained from binary collision approximation (BCA) models with good results [28,29]. Alongside experimental characterization of the linear growth rates [30,31], the crater function modeling has allowed erosive and redistributive contributions to be compared across the range of incidence angles, leading to the present understanding that these mechanisms operate simultaneously to produce surface nanopatterns [24,28]. From a more "macroscopic" perspective, MD simulations carried out to calculate the ion-induced stress distribution [32–34] have motivated the development of, and been incorporated into, models of surface evolution based on ion-enhanced viscoelastic flow [35]. To date, the consideration of the stress-driven mechanisms alongside prompt erosive and redistributive effects is limited to relatively simple models of viscous flow, which do not incorporate the MD simulation results. However, recent progress in experimental characterization of surface flow and stress parameters [36] could motivate further theoretical developments in this direction.

These recent advances in the use of simulations to inform new modeling approaches are encouraging. However, a number of key knowledge gaps have yet to be addressed with atomistic simulation tools which could provide critical insights into ion-induced nanopattern formation on Si surfaces. Several particular knowledge gaps relevant to the present work are summarized as follows:

(1) *Structure of ion-damaged Si.* It is generally accepted on the basis of both simulations [16–18] and more recently experimental evidence [35] that the first few nanometers of the irradiated Si surface quickly transition to an amorphous-like state under sustained ion bombardment at low temperatures. However, the exact nature of this ion-damaged region remains uncertain. Initial investigations have been done with MD modeling [19,34] and have shown that the preexisting surface structure is always overridden. Some characterization of the modified surface layer has been performed, indicating an increase in fivefold-coordinated Si atoms, but a complete structural analysis has not been done. In particular, it is not understood how the specific nature of the ion-damaged Si structure influences the surface properties and in particular the ion-surface interaction, beyond calculations of the ion-induced stress distribution in the damaged layers [35], which have been averaged over the entire surface and do not account for local structural variations, e.g., in the vicinity of implanted particles.

(2) *Influence of the implanted ions.* In nearly all treatments thus far, the concentration of implanted ions has been assumed to contribute nearly nothing to the overall evolution of surface nanopatterns. Contrary to this assumption, it has been known in the experimental literature for quite some time that the implanted ions can not only reach a significant concentration, but can in fact form clusters or gas bubbles at sufficiently high ion beam fluences [37–39]. These implanted ion clusters have been shown to have a spatial distribution which is well correlated with the surface topography [40], indicating that the presence of the gas bubbles may contribute to high-fluence (nonlinear) evolution of surface morphology. Furthermore, results from MD simulations [13] have led to the conjecture that these accumulated clusters can contribute to the surface evolution, e.g., by an increase in the sputtering yield due to increased surface stress leading to a "push-out" mechanism. Besides this, it can reasonably be expected that the presence of gas bubbles will lead to highly localized pressure/stress gradients within the irradiated layer. However, while the stress distribution has been treated in broad terms, the effect of the implanted ions has yet to be considered.

Only very recently has the effect of implanted particles been given notable theoretical consideration. A new model has been introduced [41] and parametrized using Monte Carlo simulations [42], which effectively treat the ion implantation as an inversion of physical sputtering, i.e., contributing a positive change in the surface height near the ion impact point. Using this treatment, the resulting formulation is conceptually similar to the Bradley-Harper theory, with angle-dependent coefficients derived from the crater function formalism. From this model, it has been shown that the effect of ion implantation is stabilizing at low angles of incidence, but generates a parallel-mode instability for higher angles. This theory was developed for the singular case of self-implantation, where the target and incident species are the same [41], but has been partially extended to consider special cases of non-self-implantation such as noble gas ions incident on C or Si surfaces [42]. While this work represents a significant step, there are still some limitations in the approach. For example, in the case of non-self-implantation, no treatment is given to clustering effects or changes due to the altered composition of the surface layer, even though the latter of these has been shown by Bradley [43,44] to be important even when no chemical bonding occurs. Further discussion to this effect is reserved for a later point in the present work.

(1) *Quantitative gaps in theoretical predictions.* Recent theoretical developments, while initially claiming excellent agreement with experimental results, have been shown by further analysis to be limited in their ability to generate quantitative predictions, which are needed in order for any model to be of use in the experimental arena. The crater function theory of Norris [25], for example, underestimates the critical angle for the flat-to-ripple transition. While criticisms of the model have offered possible explanations for the discrepancy [26,27], the same underestimate seems to be apparent when the crater functions are introduced into a kMC model [24] without the inconsistent mathematical context. As another example, the model of Castro and Cuerno [9] claims to show excellent agreement in prediction of the ripple wavelength; further analysis [10] shows that a key parameter to obtain this agreement

was in fact calculated incorrectly. Additionally, the model fails to predict an apparent leveling or slight increase in the ripple wavelength at $\sim 70^\circ$ incidence, an inconsistency which is not corrected in more recent work [35]. To address this knowledge gap in a general sense, it is not enough to simply perform atomistic simulations by themselves; rather, the approach to analysis of the simulation results must be independent of any assumptions about the mechanisms involved or for which the data are used to calculate model coefficients.

In this work, results are presented and discussed for MD simulations of cumulative low-energy ion bombardment of Si up to a "quasi-steady-state" defined by the concentration of implanted ions. Simulation parameters range across various ion energies (20–1000 eV), incidence angles ($0-85^\circ$), and species (Ne, Ar, Kr, Xe). The use of MD enables a more-or-less complete description of the atomic physics and ion-surface interaction without limiting the analysis to only a subset of the possible mechanisms. The surface is initially crystalline, which can enable the fluence-dependent characterization of the surface structure over time. In contrast with previous simulations [19] which only considered the depth profile of the implanted ions, the present data are analyzed by treating the ions as a compositional impurity; i.e., the formation and behavior of separate "phases" (i.e., clusters) of the ion species are explicitly included in the analysis. By doing this, the scope of ion-induced driving mechanisms considered by the analysis is expanded beyond the traditional single-component assessments which include sputtering, mass redistribution, and surface stress distributions.

The critical findings of this work pertain to the formation and behavior of the implanted ion clusters beneath the Si surface. The prevalence and size of these clusters are parametrized with respect to the incident ion energy, angle, and mass. In particular, the angular dependence of the ion implantation and cluster formation is found to be fairly small for low angles, but the magnitude of implantation and clustering decreases significantly for incidence angles above 45°, in the same regime where the critical angle for flat-to-ripple transitions is found. It is found that the ion clusters undergo highly localized, "explosive" degassing events as the Si layers above them are eroded and the clusters are exposed to vacuum. These degassing events lead to an enhanced rate of emission of the implanted species and thus lower the steady-state implanted ion concentration, compared to expectations from binary collision simulations. Additionally, cluster degassing is conjectured to contribute a stabilizing effect with respect to potential nanopattern formation at the surface by disrupting and destroying emergent nanopattern "seeds" before they can evolve into periodic nanostructures. In particular, Ne implantation and clustering occurs at a much greater rate compared to heavier ion species (Ar, Kr, Xe), implying that this mechanism may play a role in explaining why ion beam patterning of Si with Ne has proven so difficult in the experimental literature.

The analysis given in this work focuses primarily on the formation of ion clusters, their characterization with respect to the experimental ion beam parameters, and their direct interaction with the material surface. Additional results regarding the effect of the gas bubbles in terms of pressure or stress distribution as applied to the Si surface will be detailed in a future paper.

II. METHODOLOGY

Molecular dynamics (MD) simulations are used to observe the behavior of implanted noble gas ions after bombardment onto the (001) surface of initially crystalline silicon. LAMMPS [45] is used for MD simulations. Stillinger-Weber (SW) [46] and a hybrid Tersoff/Ziegler-Biersack-Littmark (ZBL) potential [47,48] were considered for silicon-silicon interactions and Molière [49] and ZBL [48] potentials were considered for ion-ion and ion-silicon interactions. The sputtering yield given by each combination potential was calculated at 20, 50, 100, 200, 500, and 1000 eV and compared with experimental measurements. For further simulations, SW is used for silicon-silicon interactions and ZBL is used for ion-ion and ion-silicon interactions.

The target material in all simulations is a $7.60\ \text{nm} \times 7.60\ \text{nm} \times 7.60-9.78\ \text{nm}$ block of silicon with periodic boundaries in the x and y directions and the (001) plane exposed to vacuum above the material. The target atoms are initially given random velocities to simulate a temperature of 300 K. The bottom layer of unit cells is held fixed, and a Berendsen thermostat [50] with a temperature of 300 K is applied to the next two lowest layers. Ions are created with random x and y values above the surface and given a velocity determined by the desired energy and angle of incidence to be simulated, as shown in Fig. 1. A dynamic time step is used with a minimum of 0.1 fs and a maximum of 1 fs; the velocities and forces of each atom are computed and the duration is chosen so that no atom moves more than 1 pm in a time step. Impacts are separated by 20 000 time steps, allowing the surface to equilibrate after each impact, and a snapshot of the simulation is output the time step before each impact.

Simulations vary three parameters individually: ion species, ion energy, and angle of incidence. The species simulated are neon, argon, krypton, and xenon, each at normal incidence and 500 eV. Argon at normal incidence is also simulated at 20, 50, 100, 200, and 1000 eV. 500 eV argon is simulated at 20, 40, 45, 50, 60, and 85 degrees. 500 eV neon is simulated at 45 and 60 degrees. To investigate the higher-fluence behavior of implanted ions, simulations with certain parameters are run for more impacts. 500-eV, normally incident argon is run to a fluence of $10^{16}\ \text{cm}^{-2}$, 500-eV argon at 20, 40, 45, 50, and 60 degrees is run to $3 \times 10^{15}\ \text{cm}^{-2}$, and 500-eV neon at 45 and 60 degrees is also run to $3 \times 10^{15}\ \text{cm}^{-2}$.

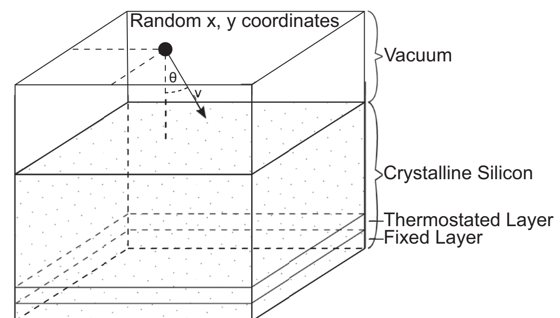

FIG. 1. Design schematic showing the division of the simulation cell into functional regions. Sputtered and reflected particles are removed from the top of the simulation cell. The azimuth of the ion trajectory relative to the surface is always in the $+x$ direction.

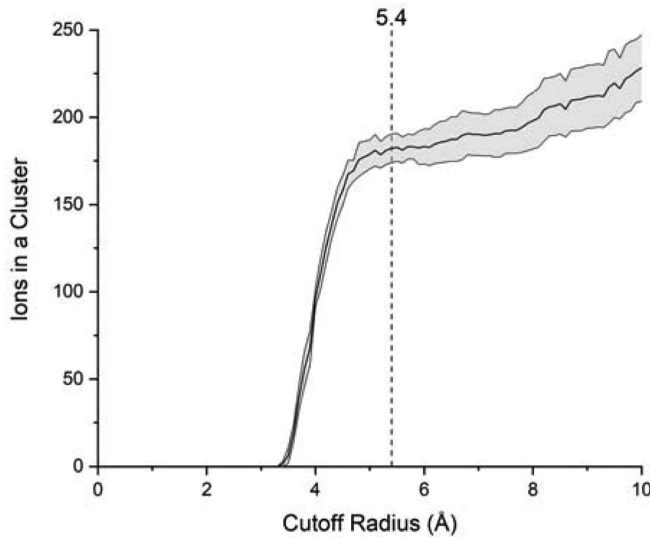

FIG. 2. Method used to select the cutoff distance between implanted ions. The cutoff is calibrated such that the number of implanted ions in clusters is insensitive to small changes in the cutoff distance. Averaged over four surfaces with implantation of 250–320 ions, the shaded gray area is standard error.

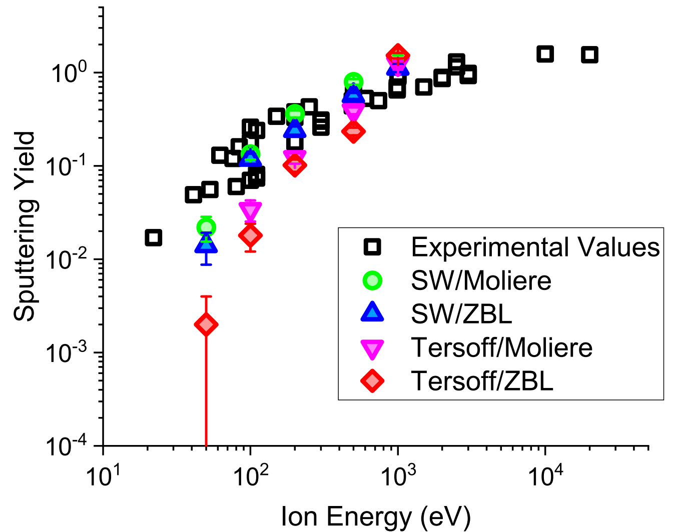

FIG. 3. Validation of potentials using calculated sputtering yields. Data in black and white are from experimental literature [53–57], while simulation results are in color. The combination of the SW potential (for Si-Si interactions) and the ZBL potential (for Ar-Ar and Ar-Si interactions) gives the best overall agreement with experimental data.

Clusters or bubbles of noble gas ions are identified by finding groups of neighboring ions, defined as ions which are separated by a distance of less than 5.4 Å. To calibrate this cutoff distance, its value was varied and the cluster identification algorithm was run for several different samples. The number of atoms included in clusters was stable around the selected value, as illustrated by Fig. 2. Clusters are also visually identified by large regions in the surface containing no silicon, using OVITO [51] to visualize the surface. Clustering data are obtained at each time step for each simulation and the results are averaged over time past a fluence of 1×10^{15} cm^{-2}, where all simulations were at or near a steady state in implantation. To obtain the percentage of implanted ions that are in a cluster, only clusters containing more than 5 ions are included, a value selected for its agreement with visualizations and being near the mean cluster size for most samples. The error in cluster size and percentage is the standard deviation of the values for all time steps. The error in steady-state composition is the standard deviation of the instantaneous concentration values from the steady-state value.

III. RESULTS

A. Validation and selection of interatomic potentials

Numerous MD studies of Si ion irradiation have been performed with several different interatomic potentials, including Stillinger-Weber (SW) [14], Tersoff [52], and environment-dependent (EDIP) [25] potentials. While some works have even directly compared these potentials [18], there is no clear consensus as to which potential gives the best or most accurate results. For the present work, the choice of potentials was made by comparing the sputtering yield of argon normally incident on a crystalline silicon surface from each combination of potentials with experimental data [53–57], using ion energies 20 eV to 1 keV. Figure 3 shows the results of these simulations compared to experimental yield data. Using the Tersoff potential for Si-Si interactions consistently underestimated the sputtering yield, so the SW potential was chosen. For ion-ion and ion-silicon interactions, the Molière potential provided higher sputtering yields than ZBL, but both were within the range of experimental values. However, the ZBL potential was closer to the mean value at 500 eV, the primary energy used, while other parameters of the simulation were varied. For all further simulations, SW and ZBL potentials were used.

It should be briefly noted that while sputtering yields were calculated for the purpose of validating potentials, studying the effects of the implanted ions on the sputtering yield was not a central consideration of this work. Such phenomena have already been reasonably well studied by previous authors [13,19], the latter of which have shown that the sputtering yield does not vary substantially with the implanted ion concentration in the early stages of irradiation.

B. Formation and characterization of clusters

Irradiation of Si(001) for varying ion energies, incidence angles, and species were simulated to fluences of at least 3×10^{15} cm^{-2}, with the fluence chosen so that all systems reached a quasi-steady-state with respect to the concentration of implanted ions. Table I summarizes the different simulation conditions studied and the key quantitative results. Note that measurements such as sputtering yield and the fraction of reflected ions have been covered extensively in the existing literature, and are not discussed any further in the present work. From early stages of irradiation, the implanted ions show a tendency to self-arrange into clusters or bubbles, with the size and predominance of these clusters varying with the simulation parameters. These clusters are exclusive volumes filled with the implanted ion species, in which no Si is present. Example

TABLE I. Summary of quantitative results from ion bombardment simulations characterizing the ion implantation and clustering behaviors. All simulations were run to a fluence of 3×10^{15} cm^{-2} or greater to achieve a quasi-steady-state concentration of implanted ions. The asterisk (*) indicates that the simulation had a deeper silicon target, diluting the atomic concentration of ions.

Ion species	Ion energy (eV)	Ion angle (deg)	Steady-state composition (10^{14} ions cm^{-2})	Steady-state composition (at. %)	Ions in clusters (%)	Cluster size (number of ions)
Ar	500	0	3.68 ± 0.49	1.11 ± 0.19*	55.7 ± 12.9	10.0 ± 3.3
Ar	20	0	0.08 ± 0.02	0.03 ± 0.01	0.0	0.0
Ar	50	0	0.25 ± 0.03	0.10 ± 0.03	0.0	0.0
Ar	100	0	0.66 ± 0.10	0.23 ± 0.11	0.0	2.3 ± 0.6
Ar	200	0	1.46 ± 0.20	0.52 ± 0.18	14.8 ± 5.6	3.6 ± 0.3
Ar	1000	0	2.92 ± 0.38	1.01 ± 0.24	37.3 ± 10.1	6.3 ± 1.4
Ar	500	20	3.71 ± 0.20	1.31 ± 0.21	47.2 ± 8.4	7.3 ± 1.3
Ar	500	40	3.41 ± 0.21	1.27 ± 0.13	26.0 ± 8.8	4.8 ± 1.2
Ar	500	45	2.82 ± 0.19	1.08 ± 0.13	22.1 ± 9.1	4.1 ± 1.0
Ar	500	50	2.66 ± 0.21	1.05 ± 0.11	15.6 ± 8.8	3.4 ± 0.7
Ar	500	60	1.74 ± 0.10	0.67 ± 0.09	8.1 ± 6.5	2.6 ± 0.6
Ar	500	85	0.0	0.0	0.0	0.0
Ne	500	0	6.97 ± 0.81	2.77 ± 0.36	66.9 ± 11.4	13.8 ± 3.6
Ne	500	45	7.37 ± 0.45	2.47 ± 0.22	51.3 ± 7.7	10.0 ± 2.8
Ne	500	60	4.29 ± 0.14	1.55 ± 0.21	22.4 ± 6.8	4.3 ± 1.0
Kr	500	0	3.02 ± 0.52	1.08 ± 0.19	46.9 ± 15.3	7.6 ± 2.6
Xe	500	0	3.49 ± 0.51	1.24 ± 0.18	50.7 ± 10.4	7.9 ± 1.8

distributions of the cluster sizes are shown in Fig. 4. Figure 5 shows the 2-dimensional projected distribution of implanted ions within the Si surface for 500 eV Ne, Ar, Kr, and Xe irradiation at normal incidence, along with the compositional depth profile of the implanted ions. In each case, multiple clusters of ions can be observed within the damaged Si matrix. Figure 6 more clearly illustrates the geometry and distribution of these clusters in three dimensions by showing only the implanted ions, with clusters of six or more atoms highlighted for clarity.

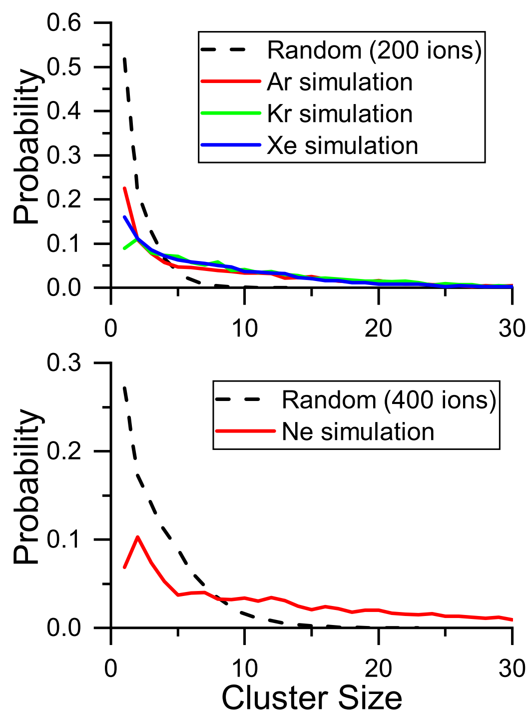

FIG. 4. The probability that an implanted ion is in a cluster of a given size. Random distributions have the same depth profile as simulations, but with a uniform random distribution of x and y coordinates. Simulated surfaces are $7 \times 7\,\mathrm{nm}^2$. All ions arrive at 500 eV and normal incidence.

To confirm that the clustering is not simply a random phenomenon, ions were generated with the same depth profile as observed in the simulated surfaces, but with completely random lateral distributions. One thousand random distributions were generated with 200 ions to compare to typical concentrations of heavier ions (Ar, Kr, and Xe), and one thousand were generated with 400 ions to compare to typical neon concentrations. All time steps that had an ion concentration within 10% of the target concentration were used to compare cluster probabilities. Figure 4 shows that for random distributions, the probability that an ion is part of a cluster rapidly approaches zero for large cluster sizes even when there is a high concentration of implanted ions. On the other hand, the number of inserted atoms which are not coordinated to any cluster is much greater for random distributions. The distributions of the simulations being studied show a different trend: the probability that an ion is in a large cluster is not negligible, even for dozens of ions.

The concentration of implanted ions, the number of ions in a cluster, and the average cluster size tend to increase with increasing energy over most of the simulated energy range. This makes sense intuitively, since very low energy ions are more likely to be reflected from the surface and

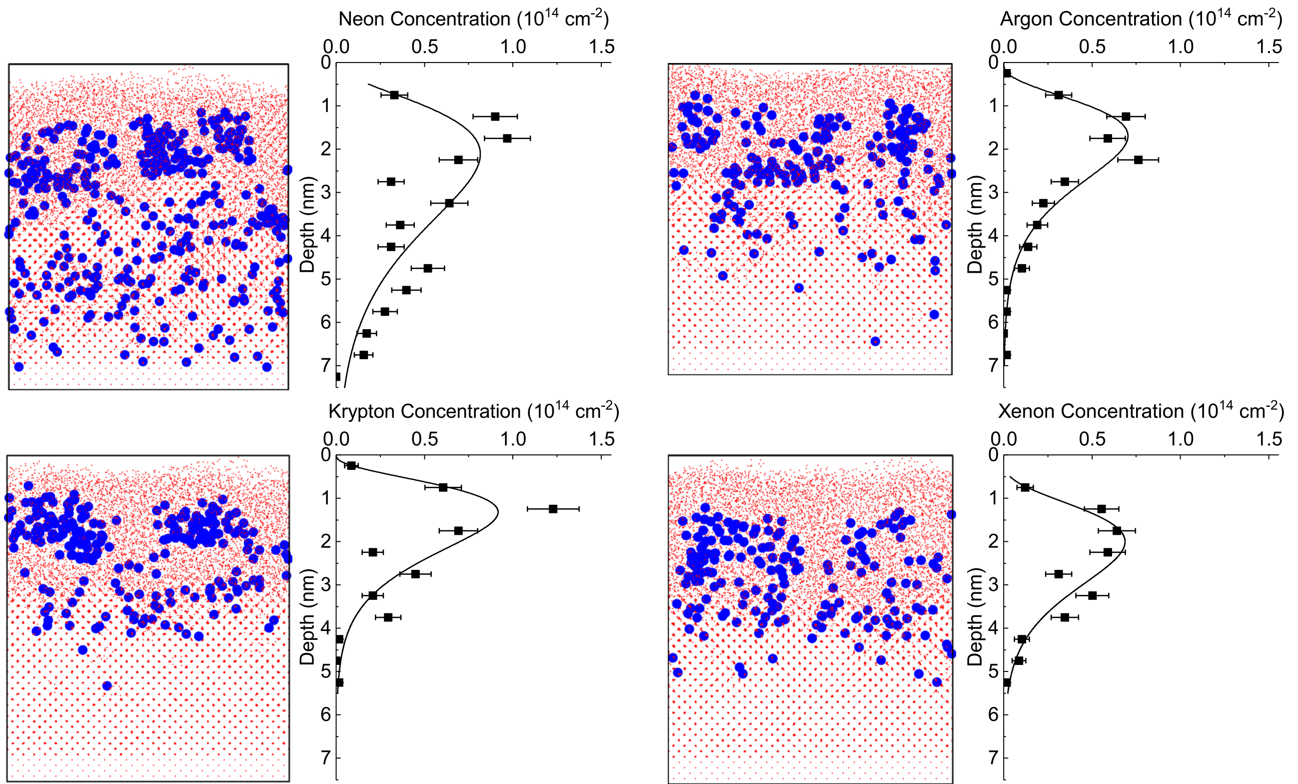

FIG. 5. Projected two-dimensional snapshots and depth profiles for each ion species at 500 eV and normal incidence. The distribution of implanted Ne is noticeably deeper and broader than for the heavier ion species.

will tend to have a very shallow implantation profile leading to very quick desorption or sputtering from later impacts. However, the same quantities actually decrease for the largest energy simulated, 1 keV (for Ar^+ incidence). This may be attributable to the increased sputtering yield having the effect of removing implanted ions at a faster rate, leaving a lower overall number of implanted ions within the surface (which could then form clusters and so on). Additionally, it is possible that the collision cascade for energies greater than 500 eV becomes increasingly linear rather than exhibiting a thermal spike behavior, and this change in the ion-surface interaction physics may also contribute, particularly to the reduced degree of cluster formation. In any case, it seems that 500 eV is close to an optimal energy for studying ion cluster formation, and this is chosen as a baseline for the remaining sets of experiments.

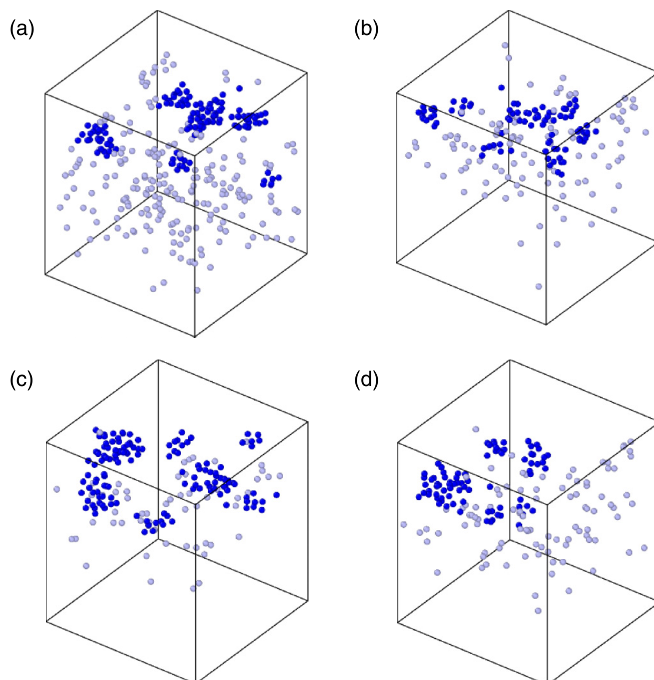

FIG. 6. Snapshots showing only the implanted ions of (a) neon, (b) argon, (c) krypton, and (d) xenon at 500 eV and normal incidence. Ions in clusters (defined as a group of six or more) are darker.

The ion concentration, fraction of ions in a cluster, and cluster size tend to decrease as the incidence angle increases, with the rate of decrease increasing for higher incidence angles. This is shown for both Ar and Ne irradiation in Table I. This behavior is also intuitive, since the reflection rate of the incident ions will increase as the incidence angle increases, leaving fewer ions to be implanted and form clusters or contribute to their growth. As discussed later, this angular dependence may have important implications for models of ion-induced nanopattern formation, since ripples are known to form on irradiated Si surfaces only for angles above a critical value $>45^\circ$ in the absence of metallic impurities [3,4].

The dependence of the implantation characteristics on the ion species, however, is not so straightforward. For the heavier-than-Si ion species (Ar, Kr, and Xe), the steady-state concentration of implanted ions and the fraction of implanted ions in a cluster both remain fairly similar for identical conditions of 500 eV normal-incidence bombardment. The

cluster size is similar for all three species, though the value for Ar is somewhat larger. However, the values for all of these implantation characteristics under Ne bombardment at the same conditions differ markedly. The steady-state concentration of implanted Ne is twice that of the other ion species, and both the percentage of ions in clusters and the average cluster size are markedly larger as well. This is presumably due to the enhanced range of Ne into Si compared to the heavier ions (∼30%–50% deeper), since Ne has a smaller atomic mass than the Si target atoms.

Since MD simulations can only access short timescales, it is necessary to confirm that the clusters are not being formed or grown by a thermal diffusion mechanism. To achieve this, the steady-state Si surface after 500 eV normal-incidence Ar^+ bombardment was allowed to run without further bombardment at 300 K for $\sim 1\ \mu s$. After this simulation was completed, the Ar atoms within the Si surface had not moved appreciably, either to grow existing clusters, to form new clusters, or to desorb from the surface. This indicates that the formation and growth of the gas atom clusters is entirely due to prompt kinetic effects from the collision cascade and/or thermal spike, and thus that the short-timescale MD treatment of the ion-surface interaction is sufficient to capture all of the relevant physics involved.

Since the clusters are not formed by diffusion, the likely mechanism for the cluster formation is kinetic trapping as the energetic ions are slowed down by interacting with the surface. Single implanted ion species tend to repel the surrounding Si atoms away to a distance of at least 3 or 4 Å, creating a potential trapping volume with an appreciable cross section. After the initial stages of the collision cascade, a newly arrived ion with some latent kinetic energy (on the order of a few eV) can travel into this trapping volume, from which it would be energetically unfavorable to escape. In fact, while the displacement energy of Si is estimated to be 10 eV or greater [58], the repulsion between two Ar atoms with the ZBL potential is less than this even for separation distances as close as 1.6 Å. Even the vacancy formation energy in Si, alone, is still calculated to be between 3.3 and 4.1 eV [59–62], while the repulsion energy between two Ar atoms at a separation of 2.0 Å is only 3.12 eV. Thus, trapping of the newly arrived ion is energetically favorable, with the resulting pressure increase leading to brief stress-driven rearrangement of the surrounding Si atoms.

C. Quasi-steady-state behavior and cluster degassing events

Figure 7 shows the evolution of the implanted ion concentration in the surface with increasing fluence up to $3 \times 10^{15}\ cm^{-2}$ for 500 eV Ar^+ irradiation. For various incidence angles, a steady-state concentration is achieved before a fluence of $2 \times 10^{15}\ cm^{-2}$ is reached. However, the steady-state concentration within the simulation cell is not constant with time, but in fact varies in a somewhat periodic manner about an average steady-state value. It should be noted that this variation is highly localized and is only observable due to the limited size of the simulation cell. Over the entire spatial domain of an experimental system, the instantaneous compositional depth profile would be approximately constant at steady state.

It is readily apparent that the steady-state implanted ion concentration decreases as the beam angle of incidence increases. This behavior is shown in Fig. 8, which shows the time-averaged quasi-steady-state ion concentration as a function of incidence angle. Interestingly, the concentration does not begin to decrease significantly until the incidence angle approaches 45°, which is well known as the critical angle for parallel-mode ripple formation on Si bombarded by Ar^+ in this energy range [3,4]. As the incidence angle continues to increase from this point, the implantation concentration decreases rapidly to near zero at grazing (∼85°) incidence.

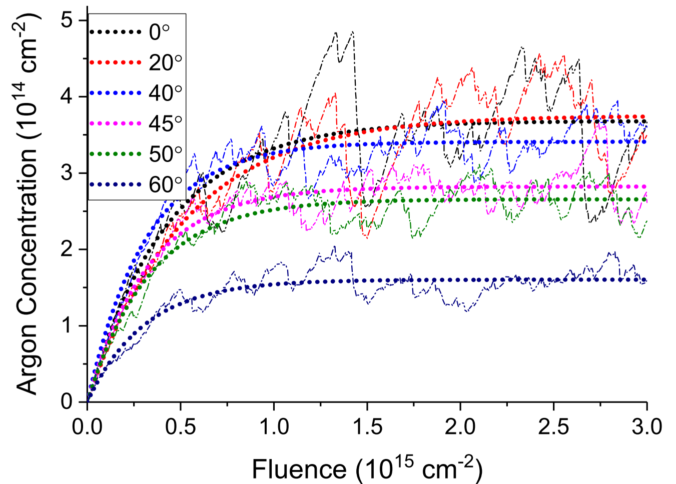

FIG. 7. Fluence dependence of the implanted ion concentration for 500 eV Ar irradiation of Si at various incidence angles up to a fluence of $3 \times 10^{15}\ cm^{-2}$. Since the concentration level exhibits oscillating behavior, the dotted lines plot a fitted average concentration to show the arrival at a quasi-steady-state for each incidence angle.

The steady-state behavior of the implanted ion composition, including the significant magnitude of the (localized) oscillations, merits closer consideration. For any ion implantation up to a high-enough fluence, a steady state is reached when

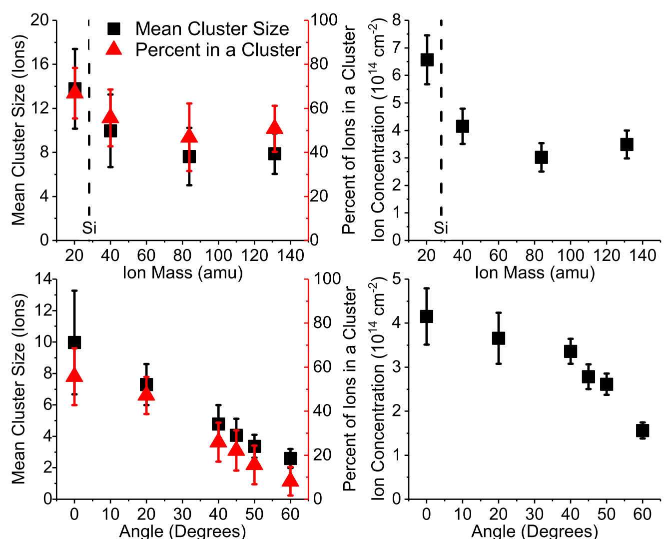

FIG. 8. Implanted ion concentrations and cluster characteristics for 500 eV irradiation of Si by each ion species at normal incidence and for Ar irradiation at various incidence angles. The values are time-averaged over the quasi-steady-state fluence range for each case.

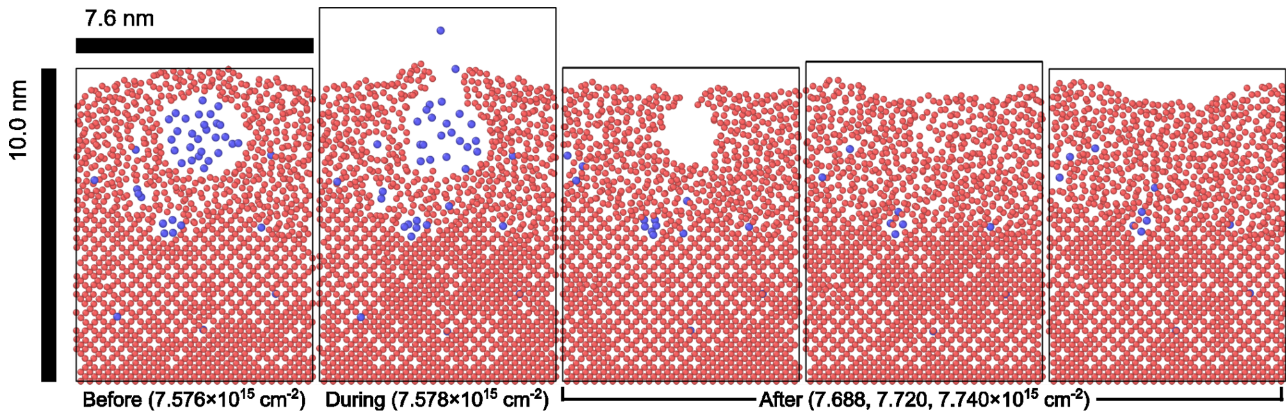

FIG. 9. Snapshots of 500 eV Ar normal incidence irradiated Si surface showing explosive decompression of a cluster: before, during (showing the cluster gas atoms evacuating), and after (showing the surface restructuring).

the incident ion flux is equal to the flux of ions emitted from the surface after its initial layers are eroded. If the implanted ions are laterally distributed with uniform probability, as is usually assumed, this emission ion flux will consist primarily of independent, single-ion removals leading to very little temporal variation in the emitted ion flux. However, in the case where the lateral distribution of implanted ions is determined by the clustering behavior previously discussed, the nature of the ion emission flux may be expected to change significantly. This is indicated clearly by the large-magnitude oscillations in ion concentration seen in Fig. 7. In fact, the drops in ion concentration are often quite sharp, indicating the rapid loss of several dozen ions from the surface.

Figure 9 graphically demonstrates the mechanism by which these sudden drops in ion concentration occur. The process occurs in four stages:

(1) The surface above a cluster of implanted ions is eroded by the incident ion flux and by sputtering and mass redistribution processes, exposing the cluster to vacuum.

(2) Now so exposed, the ions vacate the cluster in a rapid degassing event, escaping into the vacuum.

(3) A temporary void is left at the surface in place of the degassed cluster.

(4) Si atoms flow into the newly vacated void, disrupting the surface and impeding or destroying any nascent morphologies which may be present at the site of the cluster degassing event.

It should be noted that while the implanted ion clusters are exposed to vacuum due to sputtering of the Si atoms above them, the net surface recession over the course of the simulations is minimal over the fluences presented here, due to the combined effects of ion-induced swelling as well as Si sputtering.

It is particularly interesting to look at the case of Ne irradiation, given that the implanted Ne ion concentration in Si is twice that for any other species, as shown in Table I and Fig. 6. In light of this, Fig. 10 compares the implantation of the different ion species into Si at normal incidence, from which the difference in implanted concentration between Ne and the rest is not only clearly visible, but can be seen from an early stage before the concentration of either implanted species begins to stabilize. Of particular interest is the fact that the implanted concentration of Ne shows a much greater amplitude of oscillation compared to the same data for Ar implantation. Additionally, Fig. 11 shows the concentration of implanted Ne as a function of the ion fluence for 0°, 45°, and 60° incidence. It is notable that the steady-state concentration is still twice that of normal-incidence Ar even at 45°, and that the steady-state concentration for Ne implanted at 60° incidence is still appreciably greater than that for normal-incidence Ar irradiation (from Table I: 4.3×10^{14} ions/cm^2 for 60° Ne, compared to 3.7×10^{14} ions/cm^2 for 0° Ar).

Noting that Ne irradiation of Si is known not to produce nanopatterns [2] and that implantation of Ne into Si proceeds at such a notably greater magnitude compared to that of heavier ion species, the question might be raised as to whether the concentration of implanted ions plays a role in the formation of surface nanopatterns. To this end, Sec. IV B below presents a hypothetical cluster degassing mechanism which can influence surface morphology.

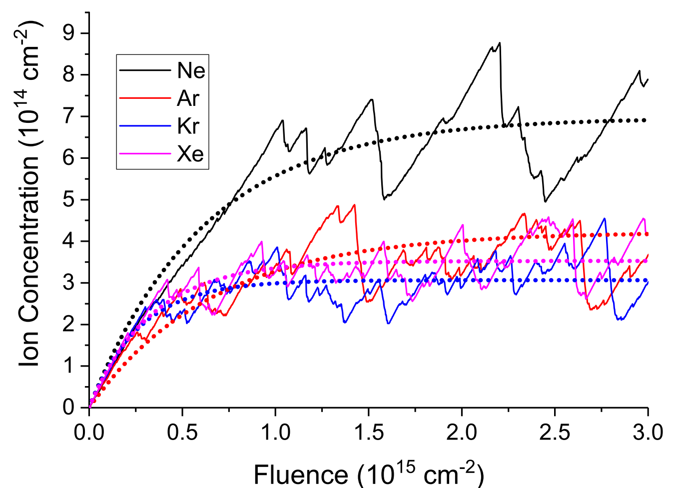

FIG. 10. Comparative plot of implanted ion concentrations for normal-incidence irradiation at 500 eV up to fluences of 3×10^{15} cm^{-2}. Ne is easily observed to implant twice as efficiently as the heavier ion species, contributing to a much stronger influence of the implanted ions.

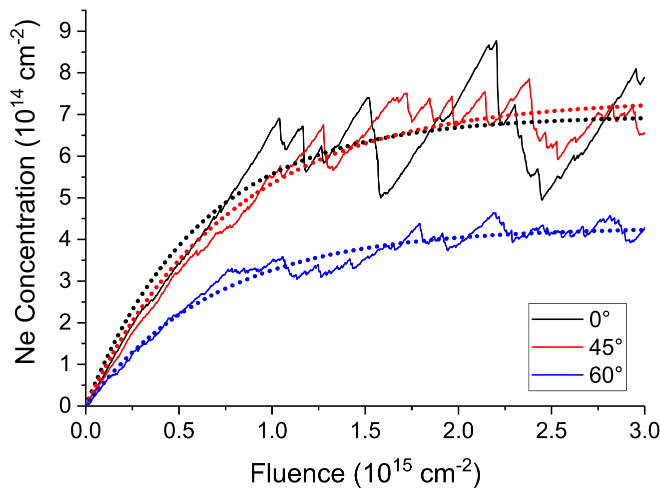

FIG. 11. Fluence dependence of the implanted ion concentration for 500 eV Ne at various incidence angles up to a fluence of 3×10^{15} cm^{-2}. The dotted lines plot a fitted average concentration to show the quasi-steady-state.

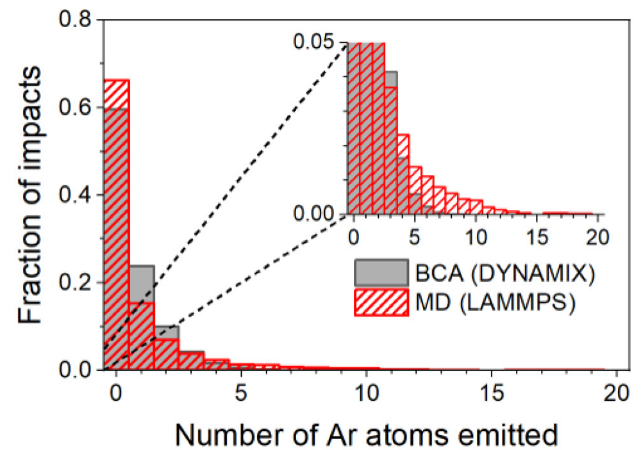

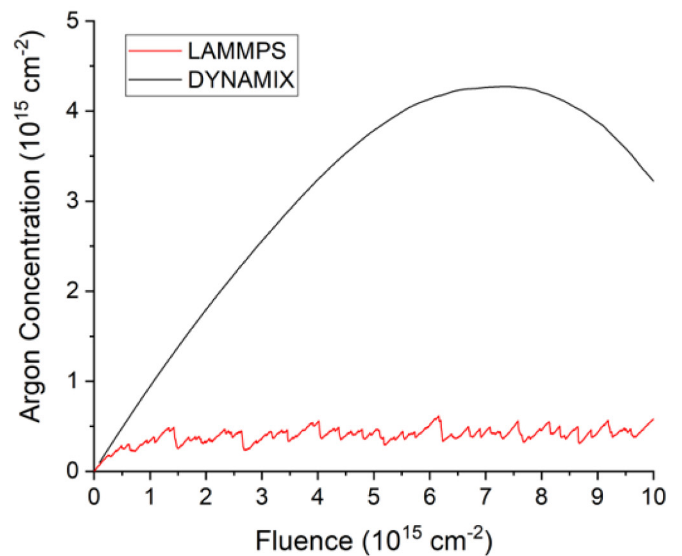

FIG. 12. Comparison of MD and BCA results for ion implantation and emission, for the case of 500 eV Ar at normal incidence. (a) Histogram of the number of Ar atoms sputtered or emitted per single-ion impact for dynamic-BCA (DYNAMIX) and MD (LAMMPS) simulations. The inset shows the same data on a reduced vertical scale. (b) Comparison of the implanted ion concentrations with respect to fluence for MD vs BCA simulations. The BCA data are plotted for every 1000 consecutive impacts, while the MD data are plotted for all 5000 impacts simulated.

IV. DISCUSSION

A. BCA vs MD

There have been some investigations comparing results for ion-surface interactions between MD and binary collision approximation (BCA) simulations [63–65]. Generally, the conclusion from these studies has been that MD simulations are able to model key effects, such as amorphization [64] or numerous small displacements [65], that BCA cannot reproduce. However, the *cumulative* implantation and emission of the ions has not been compared between these two simulation methods. Such a comparison is therefore made here, using the MD results presented above and comparing these to results from the DYNAMIX dynamic-BCA code [66]. Relevant results for this comparison are shown in Fig. 12.

Figure 12(a) compares the frequency of N-atom Ar emission events between MD (5000 impacts) and BCA (10^5 impacts) for single-ion impacts up to a fluence of 10^{16} cm^{-2}. For both BCA and MD simulations, the mode is zero, indicating that the majority of ion impacts do not lead to Ar emission from the surface for both methods. For nonzero emission events, however, the differences between BCA and MD are readily apparent. The distribution of sputtering events for the MD simulations is much broader than that of the BCA simulations. In BCA, single impacts show a much higher frequency of single-atom or few-atom sputtering events, and the largest single-impact yield of Ar atoms observed after 10^5 impacts was 11. In MD, by contrast, the distribution of Ar emission events is much broader, with emission of four or more Ar atoms from a single impact three times as frequent in MD simulations (7.9% of all events) versus the BCA simulations (2.7% of all events). Not only is this "fat tail" of the distribution more substantial for the MD simulations, but larger single-impact Ar emission yields are observed compared to BCA, with 20 single-ion impacts (0.4% out of 5000) causing emission of 12 or more Ar atoms, with the largest observed event being the emission of 35 Ar atoms. The overall increase in larger-yield Ar emission events in the MD simulations is attributable to the formation and degassing of the implanted ion clusters, as discussed in Sec. III C, and represents a discrepancy between MD and BCA simulations which the latter is unable to reproduce.

This significant difference in emission of the implanted ions can be expected to cause significant differences in the implanted ion concentrations measured from MD and BCA simulations, as well. Figure 12(b) compares the fluence-dependent implanted ion concentrations between MD and BCA simulations up to a 10^{16} cm^{-2} fluence (note that the BCA data are plotted for every 1000 impacts, which is why the point-to-point variance seen in the MD curve is not present in the BCA curve). It is readily apparent that the implanted

ion concentration from the BCA simulations is up to an order of magnitude greater than that measured from the MD results, with a maximum value of $\sim 4.2 \times 10^{15}$ ions/cm^{-2} from the BCA versus $\sim 0.6 \times 10^{15}$ cm^{-2} from the MD. While it should be noted that the ion reflection fraction from MD ($\sim$4%) is much larger than that from BCA ($\sim$0.2%), the magnitude of reflection effects is nowhere near sufficient to explain the disparity in implanted ion concentrations between the two simulation methods. Thus, this disparity is attributed principally to the formation of the implanted ion clusters, which promotes an increased frequency of high-yield Ar emission events due to cluster degassing.

Additionally, it can be seen from Fig. 12(b) that the BCA simulations have yet to reach a steady-state concentration of implanted ions. This is attributable to the fact that at a fluence of 10^{16} cm^{-2}, the initial Si surface layers have been eroded, while the deeper layers in which the most Ar is implanted have only just been exposed to vacuum. This is in contrast to the clustering effects seen in the MD simulations, which leads to collection of Ar atoms nearer to the surface at much earlier fluences.

B. Proposed connection between cluster degassing and surface morphology

As noted above, implanted ion concentrations are greatest under conditions (incidence angle, ion species) which are known to not induce nanostructure formation on Si surfaces. This suggests that ion implantation and/or clustering has a stabilizing or at least pattern-inhibiting influence on the surface morphology. Here, a hypothetical mechanism is proposed which connects the degassing of implanted clusters, illustrated in Fig. 9, to disruption of the nascent surface morphology, which may inhibit pattern formation.

While pattern formation is usually understood in terms of periodic instabilities, the surface evolution under ion beam irradiation is in fact a stochastic process [67] due to the randomness inherent in both the ion impacts themselves as well as the initial surface roughness. In both experiments [68] and simulations [69,70] it can be seen that surface morphologies initially evolve in the form of small, disconnected structures which at larger fluences grow and interconnect to form periodic nanopatterns. Thus, the degassing of the ion clusters on exposure to vacuum, and the subsequent rapid mass flow from the surrounding surface matter, has the potential to disrupt these seeds before they can grow and join to form long-scale periodic patterns.

Atomistically, the proposed effect is a stochastic mechanism which could suppress pattern formation if sufficiently strong. The strength of this inhibiting mechanism would therefore depend on the frequency and magnitude of degassing events, which in turn correlates directly to the concentration of implanted ions in the surface. Since the implanted ion concentration is greatest for smaller angles, as shown in Fig. 8 , this ion cluster degassing mechanism would contribute to a lack of pattern formation at Si surfaces under near-normal ion bombardment, which agrees well with experimental literature. Conversely, implantation and clustering is less prominent at higher incidence angles, implying that the initial small perturbations at the surface would experience far fewer disruptions due to cluster degassing. This state of the surface at high incidence angles would thus promote pattern formation, also in agreement with experimental results.

It is also of interest to consider the implications of this proposed mechanism for Ne implantation into Si, since this condition is known not to cause pattern formation at any incidence angle [2]. From Figs. 10 and 11 , it can be seen that the concentration of implanted Ne for incidence angles as high as 60° is greater than that for normal-incidence Ar implantation, which implies that the effects of cluster degassing are similarly dominant under those conditions. This in turn would indicate that the proposed cluster degassing effect is quite strong for Ne bombardment of Si over nearly all incidence angles, which again agrees well with the experimental record. The potential to elucidate the rationale behind the difficulty of patterning Si with Ne ion beams is a particular point of interest for the proposed mechanism, and thus should motivate further investigations for confirmation and clarification.

Besides the speculative nature of this proposed mechanism, an additional caveat must be noted. Namely, it cannot be used as the sole basis for a complete model of nanopattern formation; the effect described above can only be considered as a stabilizing force, whereas nanopatterns require a formative instability in order to form. However, computational and mathematical models based on MD-generated crater functions [23–25,71] have somewhat underestimated the critical angle for the onset of parallel-mode pattern formation on Si. It is possible that the incorporation of the ion cluster degassing mechanism could provide the additional stabilizing force component necessary to correct the predicted value for this angle.

C. Comparison with contemporary work on ion implantation effects

The present work is not the only study which considers the effects of the implanted ions on the surface properties and morphology. The closest theoretical analog is the work of Bradley and Hofsäss, in which a linear model of crater-function formalism type is constructed [41], which has been parametrized with BCA simulation results by Hofsäss and coworkers [42]. This model treats the ion implantation as the inverse of ion-induced sputtering and neglects any compositional effects; i.e., it is only strictly valid for self-implantation of a single species. The resulting increase in surface height near the impact point can be stabilizing or destabilizing depending on the incidence angle. It should be noted that while some earlier work [44] has studied the effects of implanted ions, that work studied pattern formation using Au ions and explained the surface evolution in terms of chemical effects such as diffusion and preferential sputtering; that work is thus more closely related to the similar model by Bradley [43] for the case of impurity codeposition than to the work presented here.

The results from the present work are not directly comparable to the model of Bradley and Hofsäss, because the results given in the present work represent an atomistic study of key phenomena and mechanisms which may influence surface nanopatterning, and do not develop a complete model of ion-beam-induced nanopatterning. Besides this, the cluster-related phenomena studied here are collective effects due to the accumulation of many implanted ions, while the continuum models consider the "crater function" from isolated single-ion

impacts. Thus, the results from the computational studies can be seen as complementary to the continuum model while also filling in some knowledge gaps regarding the collective effects of ion implantation.

Despite this complementary view, however, the simulation results raise some key questions which are not resolved by the continuum theory. One of the most pressing of these questions is, What happens when the ion concentration reaches steady state? In order for a steady-state ion implantation profile to occur, the flux of ions into and out of the surface must be equal; thus any "negative sputter yield" from implantation must be equaled by sputtering or degassing of the implanted species. From the MD results, (quasi-)steady-state implantation levels are reached for a fluence $\leqslant 10^{15}$ cm^{-2}, well below the observed patterning threshold [9,31] of $\sim 10^{16} - 10^{17}$ cm^{-2} and certainly before the surface morphology reaches a corresponding steady state. Thus, before pattern formation occurs, the rates of single-impact implantation and sputtering of the implanted species are equal. In this light, the validity of the model, which only addresses the implantation, is questionable for cases of non-self-implantation since the effect of the implanted ion emission from the surface is not included in the model coefficients. In contrast, MD results presented above indicate that the localized distribution of the implanted species can lead to additional effects at the surface even once steady-state implantation has been reached. In particular, the proposed cluster degassing mechanism of Sec. IV B is effectively independent of the relative rates of ion implantation and emission.

A second knowledge gap left by the continuum theory is the effect of the implanted ions on the surface mechanical properties. Other models of surface evolution under irradiation [8,10,35] have explored the effects of stress in the irradiated layer as a driving force for pattern formation. With the possible exception of self-implantation, it is reasonable to expect that the interatomic forces from implanted ions, whether singular or in clusters, would contribute significantly to the nature of this stress distribution. While this is not included in the continuum model, which only include prompt effects of single-ion impacts, the MD simulations provide ready access to this information. Detailed analysis of the ion-induced stress and strain within the surface is beyond the scope of the present work, and is presented in a following paper.

As a final point of comparison, it should be noted that the continuum model does not account for the effect of an altered surface layer composition for non-self-implantation cases; this can be an important contribution even if no chemical interaction occurs between the surface and implanted species [43,44]. While not likely to be a significant contribution for the cases studied both by those models and in this work (i.e., noble gas ion implantation), the MD simulations have the advantage that any such contribution is intrinsically included. This should be an additional point of consideration for future investigations.

V. CONCLUSIONS

MD simulations of cumulative ion bombardment into Si have been carried out to understand the role of the implanted ions in restructuring of Si and their contribution to nanopattern formation at the surface. Specifically, initially crystalline Si(001) has been bombarded to a fluence of 3×10^{15} cm^{-2} for a range of ion energies (20–1000 eV), incidence angles ($0-85^{\circ}$), and species (Ne, Ar, Kr, and Xe). For the majority of these conditions, the implanted ions tend to form clusters beneath the surface. The concentration of implanted ions and the prevalence of the clusters decrease as the incidence angle increases, and remain fairly similar for the heavier-than-Si ion species. However, Ne irradiation leads to significantly higher concentrations of implanted ions and increased cluster formation and size compared to the other ion species studied.

At sufficiently high fluences, the ion clusters are exposed to vacuum by the continual erosion of the Si layers, and undergo rapid degassing from the surface. This not only disrupts the surface, but also leaves a void which is quickly filled by an inward flow of amorphous Si. Furthermore, cluster degassing significantly affects the distribution of implanted ion emission events from single impacts. The distribution of these events from MD shows an elevated frequency and size of multiple-ion emissions from a single impact, compared to results from BCA simulations performed under the same conditions. This finding challenges the intuitive expectation that the number of sputtered ions per impact would be narrowly distributed under steady-state conditions. Furthermore, comparison of the MD and BCA results indicates that the effect of cluster degassing causes the steady-state implanted ion concentration to be an order of magnitude lower in MD simulations than it is in BCA simulations. Thus, the formation and emission of implanted ion clusters leads to observable differences in the MD simulations which cannot be reproduced by BCA simulations. This should be considered for future computational investigations of ion surface interactions, particularly as a key factor in the decision of whether to use MD or BCA codes for these studies.

The cluster degassing phenomenon may also provide an antipatterning influence at the surface by disrupting very early stage structures before they can grow and self-organize into periodic ripple formations. This effect could contribute a stabilizing force term to multiscale models of surface evolution, improving, e.g., the prediction of critical transition angles for pattern formation in some cases. Additionally, this effect would be active at an enhanced level in Ne-irradiated Si due to the much greater implantation and cluster formation of Ne ions, which could explain the difficulty of obtaining patterns on Ne-bombarded Si surfaces. This proposed mechanism should motivate additional theoretical and computational investigations to clarify its existence and to accurately quantify its magnitude, e.g., by parametrization with respect to the crater function formalism for direct comparison to other relevant ion-induced mechanisms.

The implications from this work may also drive new lines of experimental investigation. For example, experimental work motivated by these results can focus on confirming the relative differences in ion implantation profiles for different experimental parameters. Measurements of the implanted ion concentration done *in operando* can be carried out to confirm the prediction from MD simulations compared to BCA-based intuition. Additionally, the potential impact of the cluster degassing effect on the surface evolution can be studied with codeposition experiments using metallic impurities. These systems are known to produce patterns even at low angles of incidence for sufficiently high impurity deposition flux.

Differences in the required impurity flux to induce patterning under different ion beam species can be used to quantify the relative strength of the cluster degassing effect. In particular, if the proposed cluster degassing effect is significantly stronger for Ne ion beams, a higher impurity flux would be necessary to overcome the effect and induce pattern formation.

In addition to the cluster degassing mechanism, the presence of ion clusters within the Si near-surface layers can also have significant consequences regarding the development of an ion-induced stress-strain profile in the material. These consequences will be analyzed and discussed in a future publication.

[1] J. Muñoz-García, L. Vázquez, M. Castro, R. Gago, A. Redondo-Cubero, A. Moreno-Barrado, and R. Cuerno, Mater. Sci. Eng. R **86**, 1 (2014).
[2] F. Frost, B. Ziberi, A. Schindler, and B. Rauschenbach, Appl. Phys. A **91**, 551 (2008).
[3] C. S. Madi, H. Bola George, and M. J. Aziz, J. Phys.: Condens. Matter **21**, 224010 (2009).
[4] C. S. Madi and M. J. Aziz, Appl. Surf. Sci. **258**, 4112 (2012).
[5] R. M. Bradley and J. M. E. Harper, J. Vac. Sci. Technol. A **6**, 2390 (1988).
[6] A. Keller and S. Facsko, Materials **3**, 4811 (2010).
[7] G. Carter and V. Vishnyakov, Phys. Rev. B **54**, 17647 (1996).
[8] M. Castro and R. Cuerno, Appl. Surf. Sci. **258**, 4171 (2012).
[9] M. Castro, R. Gago, L. Vázquez, J. Muñoz-García, and R. Cuerno, Phys. Rev. B **86**, 214107 (2012).
[10] S. A. Norris, Phys. Rev. B **86**, 235405 (2012).
[11] R. Smith, D. E. Harrison, Jr., and B. J. Garrison, Phys. Rev. B **40**, 93 (1989).
[12] M. E. Barone and D. B. Graves, Plasma Sources Sci. Technol. **5**, 187 (1996).
[13] J. E. Rubio, L. A. Marques, L. Pelaz, M. Jaraiz, and J. Barbolla, Nucl. Instrum. Methods Phys. Res. B **112**, 156 (1996).
[14] T. Diaz de la Rubia and G. H. Gilmer, Phys. Rev. Lett. **74**, 2507 (1995).
[15] M. Kitabatake and J. E. Greene, Thin Solid Films **272**, 271 (1996).
[16] M.-J. Caturla, T. Díaz de la Rubia, L. A. Marqués, and G. H. Gilmer, Phys. Rev. B **54**, 16683 (1996).
[17] B. Weber, K. Gärtner, and D. M. Stock, Nucl. Instrum. Meth. Phys. Res. B **127/128**, 239 (1997).
[18] J. Nord, K. Nordlund, and J. Keinonen, Phys. Rev. B **65**, 165329 (2002).
[19] M. C. Moore, N. Kalyanasundaram, J. B. Freund, and H. T. Johnson, Nucl. Instrum. Methods Phys. Res. B **225**, 241 (2004).
[20] E. Chason, W. L. Chan, and M. S. Bharathi, Phys. Rev. B **74**, 224103 (2006).
[21] A. K. Hartmann, R. Kree, and T. Yasseri, J. Phys.: Condens. Matter **21**, 224015 (2009).
[22] B. Liedke, K. H. Heinig, and W. Möller, Nucl. Instrum. Methods Phys. Res. B **316**, 56 (2013).
[23] Z. Yang, M. Lively, and J. P. Allain, Nucl. Instrum. Methods Phys. Res. B **307**, 189 (2013).
[24] Z. Yang, M. A. Lively, and J. P. Allain, Phys. Rev. B **91**, 075427 (2015).
[25] S. A. Norris, J. Samela, L. Bukonte, M. Backman, F. Djurabekova, K. Nordlund, C. S. Madi, M. P. Brenner, and M. J. Aziz, Nat. Commun. **2**, 276 (2011).
[26] J. C. Perkinson, E. Anzenberg, M. J. Aziz, and K. F. Ludwig, Phys. Rev. B **89**, 115433 (2014).
[27] M. P. Harrison and R. M. Bradley, Phys. Rev. B **89**, 245401 (2014).
[28] H. Hofsäss, Appl. Phys. A **114**, 401 (2014).
[29] H. Hofsäss, O. Bobes, and K. Zhang, J. Appl. Phys. **119**, 035302 (2016).
[30] H. Zhou, L. Zhou, G. Özaydin, K. F. Ludwig, and R. L. Headrick, Phys. Rev. B **78**, 165404 (2008).
[31] C. S. Madi, E. Anzenberg, K. F. Ludwig, and M. J. Aziz, Phys. Rev. Lett. **106**, 066101 (2011).
[32] N. Kalyanasundaram, J. B. Freund, and H. T. Johnson, J. Eng. Mater. Technol. **127**, 457 (2005).
[33] N. Kalyanasundaram, M. C. Moore, J. B. Freund, and H. T. Johnson, Acta Mater. **54**, 483 (2006).
[34] A. Moreno-Barrado, R. Gago, A. Redondo-Cubero, L. Vázquez, J. Muñoz-García, R. Cuerno, K. Lorenz, and M. Castro, Europhys. Lett. **109**, 48003 (2015).
[35] A. Moreno-Barrado, M. Castro, R. Gago, L. Vázquez, J. Muñoz-García, A. Redondo-Cubero, B. Galiana, C. Ballesteros, and R. Cuerno, Phys. Rev. B **91**, 155303 (2015).
[36] S. A. Norris, J. C. Perkinson, M. Mokhtarzadeh, E. Anzenberg, M. J. Aziz, and K. F. Ludwig, Sci. Rep. **7**, 2016 (2017).
[37] U. Bangert, P. J. Goodhew, C. Jeynes, and I. H. Wilson, J. Phys. D **19**, 589 (1986).
[38] G. N. A. van Veen, F. H. M. Sanders, J. Dieleman, A. van Veen, D. J. Oostra, and A. E. de Vries, Phys. Rev. Lett. **57**, 739 (1986).
[39] H. A. Filius, A. van Veen, K. R. Bijkerk, and J. H. Evans, Radiat. Eff. Defects Solids **108**, 1 (1989).
[40] T. K. Chini, D. P. Datta, and S. R. Bhattacharyya, J. Phys.: Condens. Matter **21**, 224004 (2009).
[41] R. M. Bradley and H. Hofsäss, J. Appl. Phys. **120**, 074302 (2016).
[42] H. Hofsäss, K. Zhang, and O. Bobes, J. Appl. Phys. **120**, 135308 (2016).
[43] R. M. Bradley, J. Appl. Phys. **119**, 134305 (2016).
[44] S. A. Mollick, D. Ghose, P. D. Shipman, and R. Mark Bradley, Appl. Phys. Lett. **104**, 043103 (2014).
[45] S. Plimpton, J. Comput. Phys. **117**, 1 (1995).
[46] F. H. Stillinger and T. A. Weber, Phys. Rev. B **31**, 5262 (1985).
[47] J. Tersoff, Phys. Rev. B **37**, 6991 (1988).
[48] J. F. Ziegler, J. P. Biersack, and U. Littmark, *The Stopping and Range of Ions in Solids* (Pergamon Press, New York, 1985).
[49] G. Molière, Z. Naturforsch. A **2**, 133 (1947).
[50] H. J. C. Berendsen, J. P. M. Postma, W. F. van Gunsteren, A. DiNola, and J. R. Haak, J. Chem. Phys. **81**, 3684 (1984).
[51] A. Stukowski, Model. Simul. Mater. Sci. Eng. **18**, 015012 (2010).
[52] M. Koster and H. M. Urbassek, Nucl. Instrum. Methods Phys. Res. B **180**, 299 (2001).
[53] N. Laegreid and G. K. Wehner, J. Appl. Phys. **32**, 365 (1961).
[54] P. C. Zalm, J. Appl. Phys. **54**, 2660 (1983).

[55] J. W. Coburn, H. F. Winters, and T. J. Chuang, J. Appl. Phys. **48**, 3532 (1977).
[56] J. M. E. Harper, J. J. Cuomo, P. A. Leary, G. M. Summa, H. R. Kaufman, and F. J. Bresnock, J. Electrochem. Soc. **128**, 1077 (1981).
[57] P. C. Zalm, L. J. Beckers, and F. H. M. Sanders, Nucl. Instrum. Methods **209–210**, 561 (1983).
[58] L. A. Miller, D. K. Brice, A. K. Prinja, and S. T. Picraux, Phys. Rev. B **49**, 16953 (1994).
[59] S. Dannefaer, P. Mascher, and D. Kerr, Phys. Rev. Lett. **56**, 2195 (1986).
[60] P. E. Blöchl, E. Smargiassi, R. Car, D. B. Laks, W. Andreoni, and S. T. Pantelides, Phys. Rev. Lett. **70**, 2435 (1993).
[61] M. Tang, L. Colombo, J. Zhu, and T. Diaz de la Rubia, Phys. Rev. B **55**, 14279 (1997).
[62] M. J. Puska, S. Pöykkö, M. Pesola, and R. M. Nieminen, Phys. Rev. B **58**, 1318 (1998).
[63] D. Stock, M. Nitschke, K. Gartner, and T. Kandler, Radiat. Eff. Defects Solids **130–131**, 67 (1994).
[64] S. M. Foiles, *Comparison of Binary Collision Approximation and Molecular Dynamics for Displacement Cascades in GaAs* (Sandia National Laboratories, Albuquerque, 2011).
[65] L. Bukonte, F. Djurabekova, J. Samela, K. Nordlund, S. A. Norris, and M. J. Aziz, Nucl. Instrum. Methods Phys. Res. B **297**, 23 (2013).
[66] G. Hou, *The Development of a Dynamic Radiation-Surface Interaction Simulation Code* (Purdue University, 2010).
[67] T. M. Mayer, E. Chason, and A. J. Howard, J. Appl. Phys. **76**, 1633 (1994).
[68] D. Datta, S. R. Bhattacharyya, T. K. Chini, and M. K. Sanyal, Nucl. Instrum. Methods Phys. Res. B **193**, 596 (2002).
[69] Y. Ishii, W. L. Chan, and E. Chason, Nucl. Instrum. Methods Phys. Res. B **272**, 188 (2012).
[70] Z. Yang, *Development of a Multiscale Atomistic Code to Investigate Self-Organized Pattern Formation Induced by Ion Irradiation* (Purdue University, 2013).
[71] N. Kalyanasundaram, J. B. Freund, and H. T. Johnson, J. Phys.: Condens. Matter **21**, 224018 (2009).